Strain-controlled magnetic and optical properties of monolayer 2H-TaSe$_2$

Sugata Chowdhury,[1,2] Jeffrey R. Simpson,[1,3] T. L. Einstein,[4] and Angela R. Hight Walker[1]

[1]*Physical Measurement Laboratory, National Institute of Standards and Technology Gaithersburg, Maryland, 20899, USA*
[2]*Materials Measurement Laboratory, National Institute of Standards and Technology Gaithersburg, Maryland, 20899, USA*
[3]*Department of Physics, Astronomy, and Geosciences, Towson University, Towson, Maryland, 21252, USA*
[4]*Department of Physics and Condensed Matter Theory Center, University of Maryland, College Park, Maryland, 20742, USA*

First-principles calculations are used to probe the effects of mechanical strain on the magnetic and optical properties of monolayer (ML) 2H-TaSe$_2$. A complex dependence of these physical properties on strain results in unexpected spin behavior, such as ferromagnetism under uniaxial, in-plane, tensile strain and a lifting of the Raman-active E' phonon degeneracy. We predict the noncollinear magnetic phase below 6% strain and a ferromagnet above 6% strain for some types of strain. While ferromagnetism is observed under compression along $\hat{x}$ and expansion along $\hat{y}$, no magnetic order occurs when interchanging the strain direction. The calculations show that the magnetic behavior of the system depends on the exchange within the 5d orbitals of the Ta atoms. The magnetic moment per Ta atom persists even when an additional compressive strain along the $\hat{z}$ axis is added to a biaxially strained ML, which suggests stability of the magnetic order. Exploring the effects of this mechanical strain on the Raman-active phonon modes, we find that the E'' and E' modes are red shifted due to Ta-Se bond elongation, and that strain lifts the E' mode degeneracy, except for the symmetrical biaxial tensile case. The electron-phonon interactions depend on both the amount of applied strain and the direction. Additionally, we note that the charge density wave (CDW) phase weakens the magnetism due to symmetry breaking and atomic displacements (Ta atoms) depending on the type and amount of applied strain. Phonon dispersion calculations confirm that using mechanical strain we can manipulate the unique CDW phase of ML-2H-TaSe$_2$. Our results support the possibility of tuning the properties of two-dimensional transition metal dichalcogenide materials for nanoelectronic applications through strain.

I. INTRODUCTION

Two-dimensional (2D) layered materials have been the subject of intensive research due to their properties [1–8]. Among them graphene has been investigated most extensively. Electrical mobility and the Young's modulus of graphene are extremely high [9], yet its band gap is zero. These properties have triggered a broad search for other 2D materials for electronic applications. In particular, monolayer (ML) transition metal dichalcogenides (TMDs) are attractive because of their graphene-like, hexagonal structure [10] and versatile electronic properties [11–14]. Based on their electronic properties, ML-TMDs can be classified as insulators, semiconductors, semimetals, metals, and superconductors [3]. The electronic properties of ML-TMDs are broadly useful for fundamental and technological research. For example, ML-TMDs can be used as electrocatalysts for hydrogen production from water, electrodes in rechargeable batteries and photovoltaic cells, and field-effect transistors [8,15–20].

Experiments have shown that ML-TMDs can be fabricated by mechanical or solvent-based exfoliation methods [21,22] or produced by chemical vapor deposition [23,24] The properties of ML TMDs can be tuned by controlling chemical composition, functionalization, mechanical strain, and the application of external (electric and magnetic) fields [5,13,14,22, 25–31]. Magnetic materials are an important component of

low-dimensional nanoelectronic devices, but it is still rare to find a pristine, magnetic ML-TMD. Recently, different strategies have been proposed to introduce magnetism into TMDs, such as vacancy and impurity doping in bulk materials and edge effects in nanoribbons [10,28,32–39]. The successful fabrication of both TMD nanoribbons and TMDs with uniform defect density has proven complicated and remains an experimental challenge. Mechanical strain offers an attractive, alternative option because TMDs possess robust mechanical properties and can sustain strain of approximately 11% [40]. Several experimental and theoretical results have shown that the magnetic order in ML-TMDs [13,14,25,26,41–48] can be tuned by applying mechanical strain, and Wang *et al.* reported that optical properties can also be tuned with strain [49]. Previous theoretical work only considered symmetrical biaxial tensile [13,14,25,26] or uniaxial tensile strain [45]. Thus, considering these previous studies, it is of great interest to determine how the metallic ground state of TMDs behaves under different directional strain.

Here we report magnetic and optical properties of pristine, ML-2H-TaSe$_2$ under uniaxial and biaxial tensile strain, as well as combinations of expansion and compression along their basal planes, within the framework of density functional theory (DFT). To understand the magnetic behavior, we consider three different magnetic spin structures, namely, ferromagnetic (FM), antiferromagnetic (AFM), and noncollinear spin (canted spin), which are shown in the Supplemental
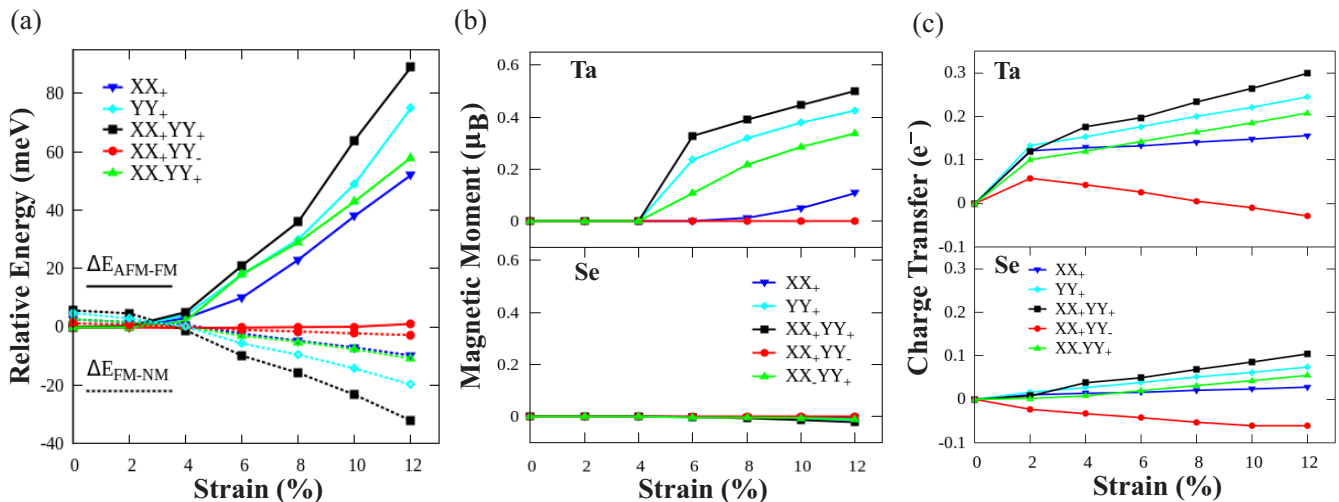
084004-1

FIG. 1. (a) The calculated energy differences per unit cell between different magnetic orders of ML-TaSe$_2$ as a function of applied strain. The energy difference between antiferromagnetic (AFM) and ferromagnetic (FM), $\Delta E_{\text{AFM-FM}} = E_{\text{AFM}} - E_{\text{FM}}$ is plotted as the top set of curves (solid), and the difference between nonmagnetic states (NM) and ferromagnetic states (FM), $\Delta E_{\text{FM-NM}} = E_{\text{FM}} - E_{\text{NM}}$, is the bottom set (dashed). The magnetic moment (b) and the electron charge transfer (c) per Ta atom (top) and per Se atom (bottom) of ML-TaSe$_2$ structures using different strain approaches.

Material (Figs. S1b–S1c) [50]. We predict a complex relationship between mechanical strain and magnetic ordering in TaSe$_2$, wherein the magnetic order depends on the strength and the direction of the applied strain.

II. RESULTS

A. Crystal structure 2H-TaSe$_2$

TaSe$_2$ has four different phases, but for this work, we will consider only its 2H phase. The trigonal prismatic structure of 2H-TaSe$_2$ is illustrated in Fig. S1a [50]. Ground state calculations are performed by relaxing the atomic position and lattice vectors of the bulk 2H-TaSe$_2$ (point group D$_{6h}$) structure. The optimized lattice constants ($a_{\text{TaSe}_2} = 0.339$ nm and $c_{\text{TaSe}_2} = 1.22$ nm) are in good agreement with previous computational studies [51,52]. Relaxed structural parameters, such as lattice constants, bond length, and intralayer distance, have been tabulated in supporting materials (Table S1) [50]. Starting with this relaxed bulk structure, we construct a ML supercell with 16-unit cells ($4 \times 4 \times 1$) and the resulting point group symmetry of D_{3h}.

B. Applied theoretical strain

The effects of strain on the supercell are modeled by stretching and compressing along the $\hat{x}$ and/or $\hat{y}$ directions, as shown in Fig. S2 [50]. In this study, we define expansion as tensile strain and the combination of expansion and compression as shear strain, following previous work [53]. The tensile strain was applied in three different ways as illustrated in Fig. S2 [50]: uniaxial expansion of ML-TaSe$_2$ in the (a) x direction (XX_+), (b) y direction (YY_+), and (c) homogeneous biaxial expansion in both $\hat{x}$ and $\hat{y}$ directions ($XX_+ YY_+$). Also, we applied two types of the shear strain (d) expansion and compression in the monolayer along the $\hat{x}$ and $\hat{y}$ directions (XX_+ YY_-), respectively, and (e) compression in the x direction and

expansion in y direction ($XX_- YY_+$) with the same magnitude of strain [50]. The theoretically applied strain varies from 0% to 12% in 2% increments. We limited the maximum strain to 12% as experiments show that nongraphene TMDs rupture once strain reaches approximately 11% [40]. Lastly, we calculate the effect of applied compression along the $\hat{z}$ direction (ZZ_-) to examine the stability of magnetic order resulting from applied biaxial strain ($XX_+ YY_+$).

C. Magnetic Properties

To study the magnetic ordering under strain, we first compare the energies of the ferromagnetic (E_{FM}), antiferromagnetic (E_{AFM}) and nonmagnetic (E_{NM}), states. Figure 1(a) shows the energy differences between E_{AFM} and E_{FM} ($\Delta E_{\text{AFM-FM}}$) and E_{FM} and E_{NM}, ($\Delta E_{\text{FM-NM}}$) as a function of mechanical strain. ML-TaSe$_2$ is a nonmagnetic system in the absence of strain. The calculated energy differences indicate that ML-TaSe$_2$ becomes ferromagnetic when uniaxial or biaxial tensile strain of 6% or larger are applied. The energy difference between AFM and FM ($\Delta E_{\text{AFM-FM}}$) is 24 meV with biaxial tensile strain of 6% and increases to 82 meV at 12%. Under shear strain the magnetic ordering is different. When expansion along the x direction and compression along the y direction are applied [Fig. S2 (d)] [50], ML TaSe$_2$ remains nonmagnetic for any amount of strain. However, ML TaSe$_2$ is ferromagnetic under 6% strain when the strain directions are interchanged [Fig. S2(e)] [50]. Recently, Manchanda *et al.* computationally investigated the magnetic properties of TaX_2 ($X =$ S, Se, and Te) [45] using biaxial strain and found similar results. Reports of several other DFT calculations also provide evidence that the magnetic properties for other TMDs can be tuned with less than 6% mechanical strain [5,13,20,25,26,54] To find the origin of this complicated relationship between applied strain and magnetic ordering in ML-TaSe$_2$, we calculated the magnetic moment and charge transfer for each atom.

Figure 1(b) displays dependence of the magnetic moment (Bohr magneton, μ_B) of each atom in TaSe$_2$ as a function of applied strain. The contribution to the magnetic moment for each Ta atom increases when the strain exceeds 6%, which is defined as the critical tensile strain [13,26,45]. At 6% biaxial tensile strain, the magnetic moment is 0.33 μ_B and increases to 0.52 μ_B at 12%. It increases with increasing biaxial and uniaxial tensile strain, as well as with shear strain XX_-YY_+ (compression along the $\hat{x}$-axis and expansion along the $\hat{y}$ axis). Finally, it is negligible when we apply tensile strain along the $\hat{x}$ axis and compression along the $\hat{y}$ axis (XX_+YY_-). The total magnetic moment arises from the Ta atoms, with a negligible contribution from the Se atoms. Additionally, we checked the magnetic moment of each Ta atom using DFT+U [55,56] with U = 2 eV. Results indicate that the magnetic moment of each Ta atom does not depend on the U value under different types of strain.

The calculated charge transfer between Ta and Se atoms is shown in Fig. 1(c). We use two different methods for charge transfer analysis: Löwdin [57,58] and Bader charge analysis [59] and achieved similar results. Here we present only the Bader charge analysis [60–62]. At 6% biaxial tensile strain, the Ta atom loses about 0.19 electrons, whereas the Se atom gains only 0.05 electrons, resulting in an increased electron density on the Ta atoms. This implies that the magnetic behavior of the system depends on the exchange between spins in the 5d orbitals of the Ta atoms. The exchange process among the 5d orbitals of the Ta atoms increases with increasing tensile strain, and it is 0.3 electrons under 12% strain. This exchange is the same under any type of applied uniaxial tensile strain and one type of shear strain XX_-YY_+. However, the system is metallic, and the exchange process among the 5d orbitals of the Ta atoms is negligible when the other XX_+ YY_- shear strain is applied.

We found that the bond length between Ta-Se atoms increases with exchange between the spins in the 5d orbitals of Ta atoms and decreases only when expansion along the $\hat{x}$ axis and compression along $\hat{y}$ axis (XX_+ YY_-) is applied (see Table S1) [50]. We conclude that the spin exchange process and bond lengthening depend on the type and direction of applied strain. Iozzi et al. [63] probed the influence of external mechanical force to break covalent bonds in a diatomic system using mechanical strain using the couple cluster method, and found that around 10% mechanical strain can rupture the covalent bonds. Recently Pan et al. [13] computationally examined the magnetic properties of VTe$_2$ under mechanical strain and considered up to 16% mechanical strain. In Fig. S3 we have shown the evolution of lattice parameters and bond lengths under various mechanical strains [50].

Now we consider the noncollinear or canted spin magnetic order below 6% applied strain. The noncollinear magnetic phase can be defined several different ways. Here we focus on the angle between the positive $\hat{z}$ and spin angle of Ta atoms (Fig. S10) [50]. In Fig. S1 and S10 we depict the Ta-atom spin angles for FM, AFM, and noncollinear magnetic phases, where the spin angle ranges from 0° to 180° in increments of 10° [50]. Here 0° represents the AFM magnetic phase and 180° represents the FM magnetic phase. The strain does not influence whether the spin is pointing up or down in the $\hat{z}$ direction. For small strain values there could be fluctuations

between them. As strain increases the barrier between up and down increases (not calculated here), so that the flip time increases rapidly, and the spins will have well-defined alignment over experimental time scales. The noncollinear magnetic behavior occurs between 0% and 6% mechanical strains. Shear strain XX_+ YY_- was not considered, because ML-TaSe$_2$ is nonmagnetic when expansion along the x direction and compression along the y direction is applied. At 2% some types of mechanical strain, the system displays noncollinear magnetism. At a spin angle of 130°, the canted spin-structure energy is lower (Fig. S11) [50], compared to other magnetic spin structures. Similarly, at 4% mechanical strain the Ta-atom spin angle is between 60° and 70° (Fig. S12) [50] and the noncollinear magnetic state energy is lower than the ferromagnetic and antiferromagnetic states. As we increase the strain the spin of Ta atoms align along the positive $\hat{z}$ axis of ML-TaSe$_2$ and the ferromagnetic spin-structure energy is lower than the canted and antiferromagnetic spin structures. This result indicates that the evolution of magnetism is a continuous process.

To understand the complex evolution of spin-structures under different types of strain, we investigate the interactions between the Ta and Se atoms in ML-TaSe$_2$. An individual Ta atom is magnetic, but covalent interactions and strong hybridization remove the Ta atom's magnetic moment. Therefore, our goal is to understand the nature of the spins in the 5d orbitals of individual Ta atoms under different types and directions of applied strain. To achieve this, we compare the partial density of states (PDOS) of unstrained and strained ML-TaSe$_2$. In Fig. 2, the red and blue regions represent the spin-up and spin-down components, respectively. In Figs. 2(a) and 2(b), we show the PDOS of the 5d orbital of Ta and the 4p orbital of the Se atom without strain (0%) and under 6% biaxial tensile strain, respectively. At the Fermi level (dashed vertical line), the PDOS decreases in the 4p states of the Se with 6% strain [Fig. 2(b)], and these states no longer take part in the hybridization process with the Ta atoms [26]. On the other hand, the spin degeneracy is broken for the 5d orbitals of the Ta atom as highlighted with arrows [Fig. 2(b)], and magnetic order is induced in the system [26]. At this Fermi level, the character of the 5d orbitals of the Ta atom is comprised of the $d_{x^2-y^2}$ and d_{xy} orbitals, which lie in the basal plane [26]. The spin-splitting exchange between these two orbitals is enhanced as the strain is increased and is directly proportional to the bond length between the Ta and Se atoms. In contrast, under XX_+ YY_- strain shown in Fig. 2(c), the Se 4p PDOS of increases and the Ta 5d PDOS decreases. In Fig. S4 of the supporting materials [50], we plot the increase and decrease of number of states for the 5d orbital of Ta and the 4p orbital of Se atoms, respectively. This result suggests that the spin polarization increases as the hybridization process between the Ta and Se atoms decreases due to biaxial strain. Finally, biaxial compressive strain leads to ML-TaSe$_2$ being a NM system due to stronger hybridization. The evolutions of PDOS under different strengths (2%– 12%) and directions of mechanical strain are shown in the supporting materials, Figs. S5– S9 [50].

Considering practical applications in nanoelectronic devices, we probe the effect of magnetic ordering with additional strain applied along the $\hat{z}$ axis. We consider two different
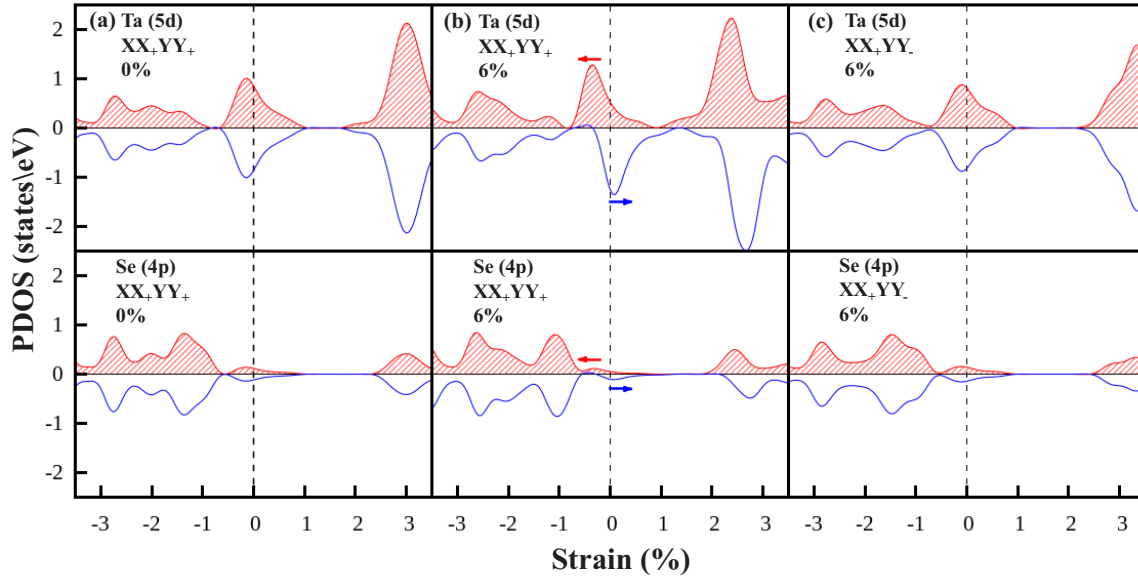
FIG. 2. Spin-polarized, partial density of states (PDOS) of Ta (top) and Se (bottom) corresponding to (a) 0%, (b) 6% symmetrical biaxial tensile strain, and (c) 6% expansion in the $\hat{x}$ direction and compression in the $\hat{y}$ direction (XX_+YY_-). Here red represents the spin up and blue represents the spin down. The Fermi level is indicated by the dashed vertical black line and the horizontal arrows highlight the spin splitting near the Fermi level, which is only nonzero in (b) for 6% biaxial strain.

situations along the z axis: (1) compressive strain along the $\hat{z}$ axis when ML-TaSe$_2$ is under no symmetrical biaxial tensile strain, and (2) compressive strain along the $\hat{z}$ axis with biaxial tensile strain at 6%. The magnetic moment (μ_B) of each Ta atom under strain along $\hat{z}$ direction at 6% symmetrical tensile strain ($XX_+ YY_+$) of ML-TaSe$_2$ is shown in Fig. 3. The magnetic moment per Ta atom is 0.09 μ_B when compressive strain is applied along the $\hat{z}$ axis without additional strain in
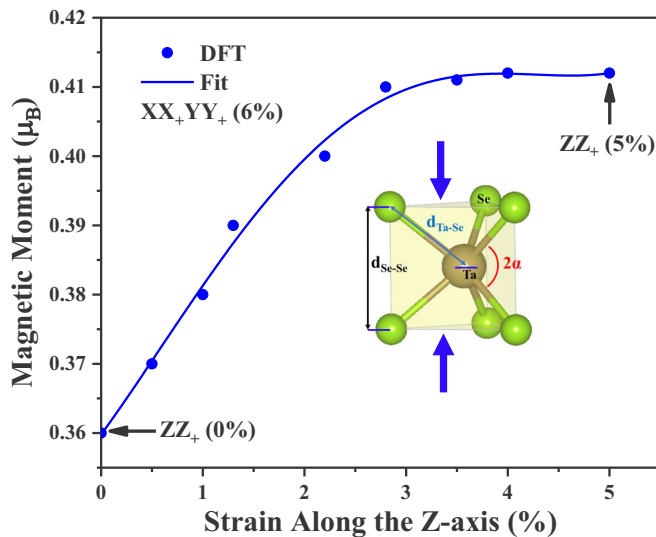

FIG. 3. Magnetic moment (μ_B) of each Ta atom under compressive strain along the direction ($\hat{z}$) perpendicular to the XY plane at 6% symmetrical tensile strain (XX_+YY_+) of ML-TaSe$_2$. Inset: the trigonal prismatic coordination of 2H-TaSe$_2$ and applied strain direction along the $\hat{z}$ axis. These results suggest that magnetism is sustained even with applied strain along the $\hat{z}$ axis. Fitting parameters are mentioned in the Supplemental Material [50].

the basal plane, and the intralayer distance between Se-Se is 0.324 nm. Under symmetrical biaxial strain (6%), the Ta magnetic moment starts at 0.33 μ_B and reduces to 0.24 μ_B when the applied strain along the $\hat{z}$ axis reduces to 5%. If we apply compression along the $\hat{z}$ axis, the magnetic order is destroyed only when this strain exceeds 5%. This implies that the magnetic order is likely enough for nanoelectronic device applications.

Also, the calculated Curie temperature (T_C) was used to probe the stability of the magnetic order at high temperature. While it is long known that mean field theory can drastically overestimate T_c in two-dimensional systems [64,65] this effect may be less problematic for long-range interactions (the non-nearest neighbor Heisenberg model) and the mean field has been routinely used in analyzing nanoparticles [26] and surfaces of magnetic systems [66]. Furthermore, even if mean-field estimates of T_c are too large, the trend should be meaningful. Thus, we estimate T_C from $k_B T_C = (2/3)\Delta E_{\text{AFM-FM}}$. Our enhanced T_C is approximately room temperature or 287 K at 8% and nearly twice that at 12% biaxial XY tensile strain. This finding suggests that ferromagnetic behavior of strained TaSe$_2$ monolayer is stable at room temperature and useful for operation of nanoelectronic devices.

D. Raman modes

In this section, we discuss the evolution of the Raman-active phonon modes of 2H-TaSe$_2$ as a function of applied mechanical strain. Raman spectroscopy provides detailed information about the lattice structure of materials among other important details. To probe the effect of strain on the Raman phonons, DFT predictions are compared with experimental results for bulk 2H-TaSe$_2$ (D_{6h}). At the Γ point, bulk 2H-TaSe$_2$ has 12 phonon modes, represented by $\Gamma(D_{6h}) = A_{1g} + 2A_{2u} + B_{1u} + 2B_{2g} + E_{1g} + 2E_{1u} + E_{2u} + 2E_{2g}$ although only four
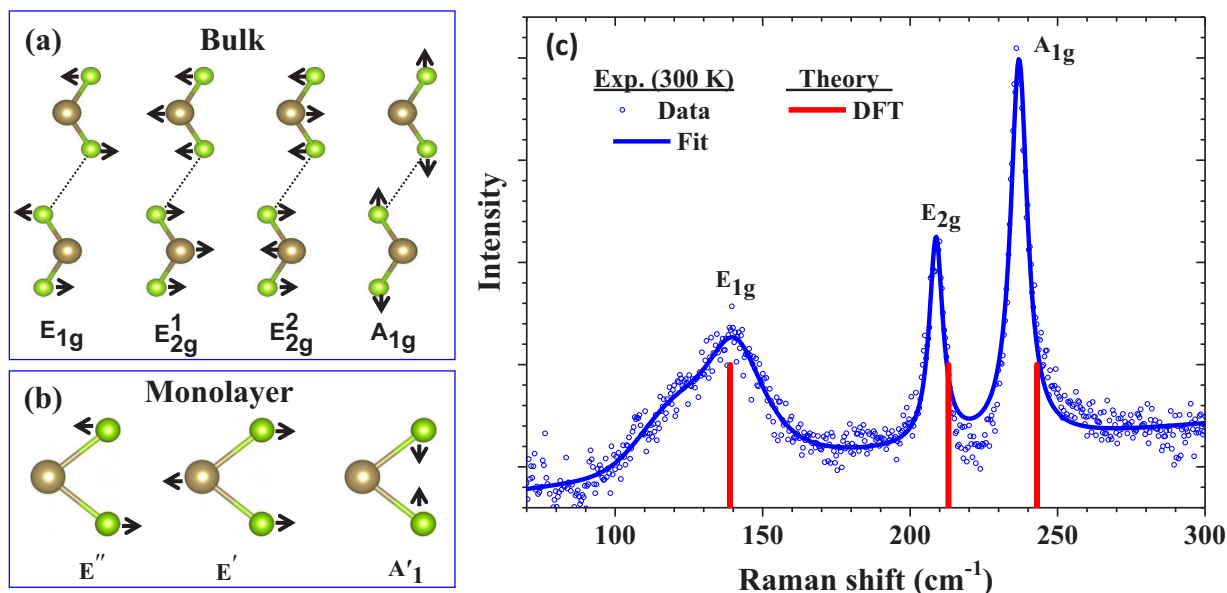
FIG. 4. Symmetry allowed Raman active modes of unstrained 2H-TaSe$_2$ for (a) bulk and (b) monolayer. (c) Comparison between Raman spectra of unstrained bulk 2H-TaSe$_2$ measured experimentally at 300 K (blue circles and blue fit line) and calculated prediction using DFT (red lines).

are Raman active: A_{1g}, E_{1g}, and $2E_{2g}$ as shown in Fig. 4(a). The Raman spectrum obtained from experiment at room temperature is shown in Fig. 4(c) with data shown as blue dots and the peak fit shown as a solid blue line. Our experimental results, in agreement with previous studies [67], show three main peak features at 140 cm^{-1}, 209 cm^{-1}, and 237 cm^{-1}. The DFT results agree well with our experiments, giving predicted values for E_{1g}, E_{2g}, and A_{1g} modes at 139 cm^{-1}, 213 cm^{-1}, and 243 cm^{-1}, providing support for our theoretical model.

Next, we examine the Γ-point phonon modes of ML-TaSe$_2$, whose optical properties are different from those of bulk 2H-TaSe$_2$ due to differences in point group and dimensionality. The point group symmetry of ML-TaSe$_2$ is D_{3h}, with six phonon modes: A_1', A_2', E', A_1'', A_2'', and E'', only three of which are Raman-active: E'', E', and A_1'. In Fig. 4(b), the Raman active modes of ML-TaSe$_2$ are shown, which corresponds to the characteristic A_{1g}, E_{1g}, and E_{2g} modes of bulk 2H-TaSe$_2$. We also compared our predictions with other theoretical predictions [52] and experimental results [67]. We predict Raman peaks at 138 cm^{-1} (E''), 210 cm^{-1} (E'), and 237 cm^{-1} (A_1'), which are in good agreement with previous reports [52,67].

Figure 5 shows the calculated frequency shifts of Raman-active phonon modes at the Γ point as a function of strain from 0% to 12% for the indicated strain configurations. Our analysis reveals that E'' is the most sensitive mode and shifts to lower frequency (red shifts) under any type of strain conditions. The magnitude of the E'' red shift depends on the direction of applied strain. The red shift of E'' is a maximum ($\sim$40 cm^{-1}) under symmetrical biaxial strain (12%) and a minimum ($\sim$10 cm^{-1}) under $XX_{+}YY$. The A_1' peak blue shifts, reaching maximum ($\sim$10 cm^{-1}) under symmetrical biaxial strain (12%). The most interesting Raman peak is E', which involves opposite vibrations of the two Se atoms with respect to the Ta atom in the basal plane [Fig. 4(b)]. The

degeneracy of E' is lifted upon application of uniaxial or pure shear strain. This doubly degenerate optical phonon mode (E') further splits into two singlet subbands, named E'^{+} and E'^{-}, respectively. There a red shift occurs to E'^{+} by approximately 40 cm^{-1} under 12% symmetrical biaxial strain.

To understand the mechanical strain effect on the optical properties of ML-TaSe$_2$, we calculated the phonon dispersion curves (Fig. 6), both without strain (0%) and under 6% strain in the indicated configurations. Changes in all Raman modes under strain are shown in Fig. S13–S17 [50]. To reduce the computational time, we considered unit cells that contain only three atoms for all ML-TaSe$_2$, which produced nine phonon bands. Out of the nine, the three acoustic branches (red in Fig. 6) are separated from the six optical branches (blue in Fig. 6) by a 20 cm^{-1}. Analyzing the phonon dispersion curves, we noticed that there are no negative phonon frequencies in the acoustic branch in the unstrained (0%) or 6% symmetrical biaxial strain [Fig. 6(a)]. Also, there is no splitting within the optical branches. Interestingly, all other kinds of strain produce negative phonon frequencies for the acoustic branches along the ΓM, MK, and KΓ directions and cause splitting in the optical branches. Negative frequencies for acoustic modes imply an atomic displacement and breaking of the symmetry of ML-TaSe$_2$. The MK direction has the largest effect. Our DFT results revealed that the symmetry of the structure is preserved and that the Ta-Ta bond length in the XY plane increases monotonically. On the other hand, the change of the Ta-Ta bond length (and its sign) depends on the mechanical strain direction. Due to the asymmetric nature of the mechanical strain, the monolayer structure is distorted and leads to a different phase of the systems. The imaginary frequency of an acoustic branch corresponds the atomic displacement and formation of superlattice in the charge density wave (CDW) phase of TaSe$_2$ at low temperature (122 K) [68]. Recently, experiments demonstrated strain manipulation of the CDW phase of 2H-NbSe$_2$ [69] 1T-VSe$_2$ [70] and 1T-TiSe$_2$ [71].
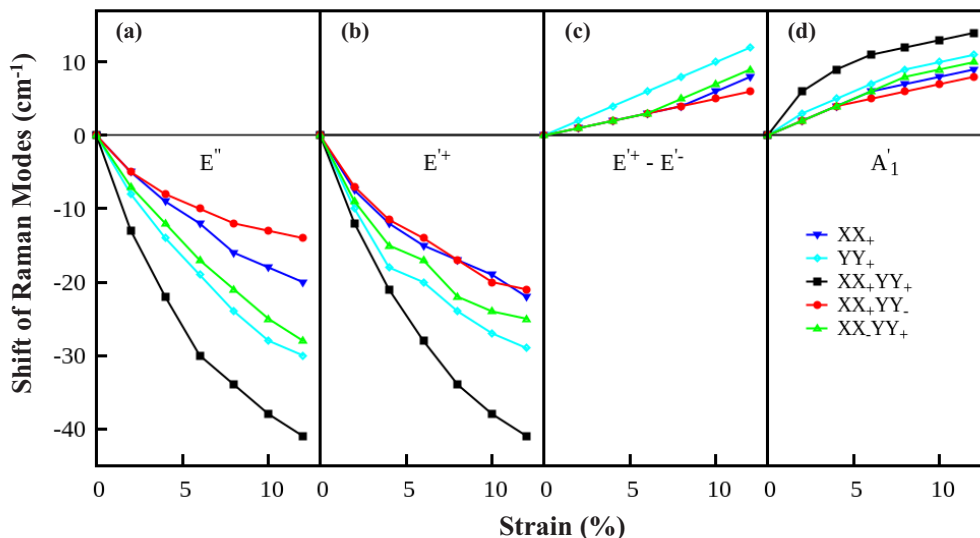
FIG. 5. The shift of the Raman modes of ML-TaSe$_2$. Panels (a) and (b) represent in-plane shearing modes E'' and E'^+, respectively, and panel (d) represents the out-of-plane mode A'_1. (c) Peak frequency difference between E'^+ and E'^-. E' is no longer degenerate, with each E' split into two modes: E'^+ and E'^-. These modes are present for all types of strain, except the symmetrical biaxial strain XX_+YY_+ (black squares).

They support our theoretical results that we can manipulate the electronic structure of the ML-TaSe$_2$ with strain, leading to the CDW phase of the structure.

Recently, Batzill and coworkers experimentally demonstrated that the ferromagnetic state in a monolayer VSe$_2$ and the CDW phase coexist at low temperature [72]. Encouraged by our phonon calculations and recent experimental evidence of monolayer VSe$_2$ [72], we investigate the structure of ML-TaSe$_2$ at low temperature. We introduced the electronic temperature by tuning the smearing factor σ which describes the Fermi-Dirac distribution so we can qualitatively assess the effect of temperature on the phonon properties of the system

[73] and the Kohn anomaly [52]. To understand the CDW phase of magnetic structure at low temperature, we considered a $3 \times 3 \times 1$ supercell of ML-TaSe$_2$ at low temperature [74]. First we investigate the atomic structure for ML-TaSe$_2$ at 10 K under no strain and found it forms a triangular structure (Fig. S18) [50], which is in excellent agreement with experimental observations [74]. Next we considered the supercell structure under different applied mechanical strain based on our phonon calculations. We excluded $XX_+ YY_+$ and $XX_+ YY_-$ [50]. The monolayer structures are shown in Fig. S19–Fig. S21 at 10 K under applied mechanical strain. Our DFT calculations revealed that under mechanical strain, a
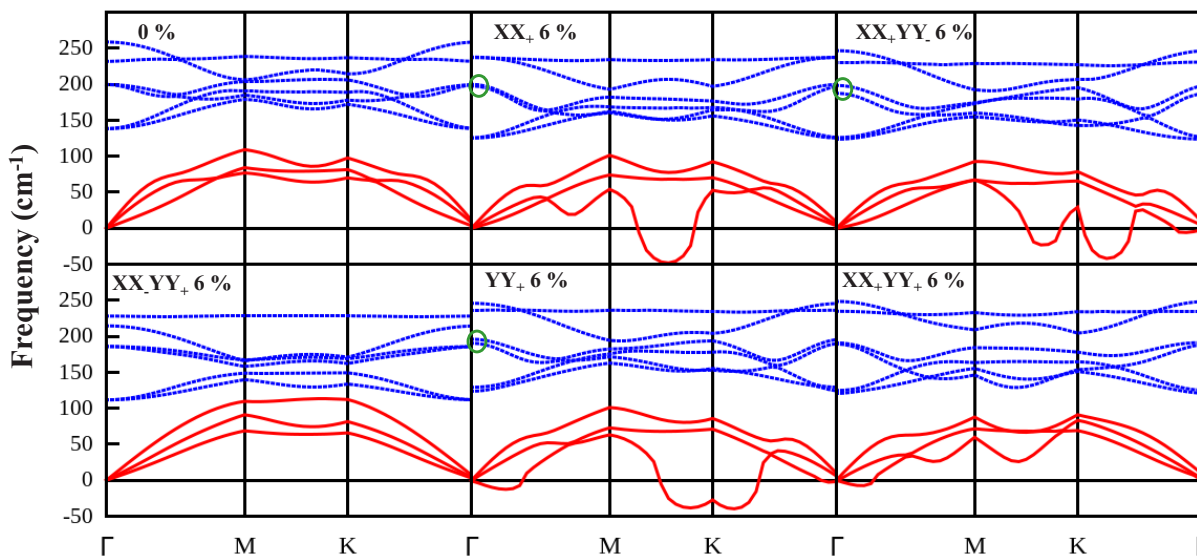

FIG. 6. Predicted phonon dispersion curves of ML-TaSe$_2$ in **k** space as a function of different types of in-plane strain compared to the unstrained system (upper left panel). Blue and red dispersion curves represent the optical and acoustic modes, respectively. The phonon dispersion curves are substantially changed compared to the unstrained and symmetrical biaxial strain case (lower left panel). Strain lifts the degeneracy of the E' mode at 184 cm^{-1} frequency in YY_+ strain (upper middle and upper right panels). Negative frequencies for acoustic modes imply instability to a distorted structure. The green circles indicate the splitting in an optical branch of the phonon dispersion.

magnetic $3 \times 3 \times 1$ supercell favored rectangular structure or stripes at low temperature. Recently we investigated the CDW phase of bulk 2H-TaSe$_2$ as a function of temperature, and our DFT found that in the commensurate phase of bulk 2H-TaSe$_2$ a striped supercell structure is formed [75]. From this result we conclude that at low temperature, mechanically strained magnetic ML-TaSe$_2$ could form a commensurate structure, although experimental validation is needed to understand the CDW phase of magnetic ML-TaSe$_2$.

III. METHODS

A. Computational

Calculations were carried out using DFT [76,77] as implemented in the PWSCF code [78], using the projector augmented wave (PAW) method [79]. The kinetic energy cutoff of the plane-wave expansion is taken as 520 eV. We used Methfessel-Paxton [80] smearing of 0.02 Ry for all calculations. All the geometric structures are fully relaxed until the force on each atom is less than 0.002 eV/Å, and the energy-convergence criterion is 1×10^{-6} eV. For the electronic-structure calculations, a $32 \times 32 \times 1$ **k**-point grid is used. To estimate the charge transfer we have used the Bader charge analysis code [60–62,81] To investigate the spin structure, we construct a $4 \times 4 \times 1$ supercell and use a sufficiently large vacuum (20 Å) in the vertical direction to render negligible any interaction between neighboring supercells. In addition to this, we also used U = 2 eV for each Ta atom in the DFT+U approach.

To understand the noncollinear magnetism, we have varied the angle between the positive $\hat{z}$ and spin angle of Ta atoms (Fig. S3). The range of angle is 0°–180° in increments of 10°. We have used fully relativistic PAW pseudopotentials [82].

For phonon calculations, we considered unit cells that contain only three atoms for all ML-TaSe$_2$, which produced nine phonon bands. We used a $4 \times 4 \times 4$ uniform q grid and $36 \times 36 \times 1$ k-point grid for vibration properties. Within the local-density approximations (LDA), we employ the Perdew-Zunger exchange and correlation functionals [83] for the phonon calculations. Here we used the LDA exchange-correlation functional because it yields a better description of the optical properties of the material than does the general-gradient approximation [84]. We considered a $3 \times 3 \times 1$ supercell to understand the CDW phase of the ML-TaSe$_2$. To model the temperature-dependent formation of the CDW states, here we used electronic temperature. The electronic temperature can be modeled by tuning the smearing factor σ, a parameter that describes the Fermi-Dirac distribution, to qualitatively assess the effect of temperature on both the phonon properties of the system and the Kohn anomaly [85,86].

B. Raman Measurements

Raman spectrum for bulk TaSe$_2$ excited with a HeNe laser at 632.8 nm (sample power <1 mW) was measured at room temperature using a triple-grating Raman spectrometer (Horiba JY T64000 with a 50X objective, N.A. 0.82) coupled to a liquid-nitrogen cooled charge-coupled device detector. All spectra were taken in the 180° backscattering configuration. The bulk TaSe$_2$ sample was freshly exfoliated.

The purpose of identifying the computer software and experimental setup in this article is to specify the computational procedure and Raman measurement. Such identification does not imply recommendation or endorsement by the National Institute of Standards and Technology.

IV. CONCLUSION

In summary, we studied the magnetic and optical properties of monolayer TaSe$_2$ under mechanical strain using spin-polarized DFT. Pristine, ML 2H-TaSe$_2$ is nonmagnetic, but becomes ferromagnetic with applied basal strain beginning at approximately 6%, except for pure shear strain, e.g., simultaneous symmetrical tensile strain along the $\hat{x}$ axis and compressive strain along the $\hat{y}$ axis. The magnetic order of metallic TaSe$_2$ depends on the direction of the applied strain. We also found a noncollinear magnetic phase below 6% strain. The calculated Curie temperature of strained TaSe$_2$ implies that the ferromagnetic ML is suitable for spintronics applications near room temperature. Most importantly, we demonstrate the stability of the magnetic order under additional strain along the $\hat{z}$ axis, a robustness that is desirable for practical applications of ML TMDs in nanoelectronic devices. The experimental Raman spectrum of bulk 2H-TaSe$_2$ and our DFT-predicted phonon frequencies are in excellent agreement. Raman calculations of strained ML-TaSe$_2$ show significant red shift of E'' and a blue shift for A_1'. We also find that the doubly degenerate E' mode splits into two components: $E^{'+}$ and $E^{'-}$, respectively. This splitting and shifting of the modes depend on the direction and magnitude of the applied strain. The phonon dispersion evaluation with respect to mechanical strain is intriguing, particularly with similarities to other CDW materials. The noncollinear magnetic state could be useful for spin-magnetic storage devices. Our work sheds light on TMD materials and their possible applications in strained devices.

[1] K. S. Novoselov, A. K. Geim, S. Morozov, D. Jiang, M. Katsnelson, I. Grigorieva, S. Dubonos, and A. Firsov, Nature (London) **438**, 197 (2005).

[2] K. S. Novoselov, A. K. Geim, S. V. Morozov, D. Jiang, Y. Zhang, S. V. Dubonos, I. V. Grigorieva, and A. A. Firsov, Science **306**, 666 (2004).

[3] M. Chhowalla, H. S. Shin, G. Eda, L.-J. Li, K. P. Loh, and H. Zhang, Nat. Chem. **5**, 263 (2013).

[4] Q. H. Wang, K. Kalantar-Zadeh, A. Kis, J. N. Coleman, and M. S. Strano, Nat. Nanotechnol. **7**, 699 (2012).

[5] H. Pan and Y.-W. Zhang, J. Mater. Chem. **22**, 7280 (2012).

[6] A. Kuc, N. Zibouche, and T. Heine, Phys. Rev. B **83**, 245213 (2011).

[7] J. Wilson, F. Di Salvo, and S. Mahajan, Adv. Phys. **50**, 1171 (2001).

[8] J. Wilson and A. Yoffe, Adv. Phys. **18**, 193 (1969).

[9] S. Ghosh, I. Calizo, D. Teweldebrhan, E. P. Pokatilov, D. L. Nika, A. A. Balandin, W. Bao, F. Miao, and C. N. Lau, Appl. Phys. Lett. **92**, 151911 (2008).

[10] C. Ataca, S. Cahangirov, E. Durgun, Y.-R. Jang, and S. Ciraci, Phys. Rev. B **77**, 214413 (2008).

[11] A. Splendiani, L. Sun, Y. Zhang, T. Li, J. Kim, C.-Y. Chim, G. Galli, and F. Wang, Nano Lett. **10**, 1271 (2010).

[12] B. Radisavljevic, A. Radenovic, J. Brivio, i. V. Giacometti, and A. Kis, Nat. Nanotechnol. **6**, 147 (2011).

[13] H. Pan, Sci. Rep. **4**, 7524 (2014).

[14] H. Shi, H. Pan, Y.-W. Zhang, and B. I. Yakobson, Phys. Rev. B **88**, 205305 (2013).

[15] W. Liang and S. Cundy, Philos. Mag. **19**, 1031 (1969).

[16] C. Lee, Q. Li, W. Kalb, X.-Z. Liu, H. Berger, R. W. Carpick, and J. Hone, Science **328**, 76 (2010).

[17] R. Kasowski, Phys. Rev. Lett. **30**, 1175 (1973).

[18] M. Benameur, B. Radisavljevic, J. Heron, S. Sahoo, H. Berger, and A. Kis, Nanotechnology **22**, 125706 (2011).

[19] R. Coehoorn, C. Haas, J. Dijkstra, C. J. F. Flipse, R. A. de Groot, and A. Wold, Phys. Rev. B **35**, 6195 (1987).

[20] H. Pan, Sci. Rep. **4**, 5348 (2014).

[21] J. N. Coleman, M. Lotya, A. O'Neill, S. D. Bergin, P. J. King, U. Khan, K. Young, A. Gaucher, S. De, and R. J. Smith, Science **331**, 568 (2011).

[22] C. Feng, J. Ma, H. Li, R. Zeng, Z. Guo, and H. Liu, Mater. Res. Bull. **44**, 1811 (2009).

[23] Y. Yu, C. Li, Y. Liu, L. Su, Y. Zhang, and L. Cao, Sci. Rep. **3**, 1866 (2013).

[24] R. J. Smith, P. J. King, M. Lotya, C. Wirtz, U. Khan, S. De, A. O'Neill, G. S. Duesberg, J. C. Grunlan, and G. Moriarty, Adv. Mater. **23**, 3944 (2011).

[25] H. Pan and Y.-W. Zhang, J. Phys. Chem. C **116**, 11752 (2012).

[26] Y. Zhou, Z. Wang, P. Yang, X. Zu, L. Yang, X. Sun, and F. Gao, ACS Nano **6**, 9727 (2012).

[27] X. Li, S. Yu, S. Wu, Y.-H. Wen, S. Zhou, and Z.-Z. Zhu, J. Phys. Chem. C **117**, 15347 (2013).

[28] C. Ataca and S. Ciraci, J. Phys. Chem. C **115**, 13303 (2011).

[29] C. Ataca, H. Sahin, E. Akturk, and S. Ciraci, J. Phys. Chem. C **115**, 3934 (2011).

[30] S. Yang, D. Li, T. Zhang, Z. Tao, and J. Chen, J. Phys. Chem. C **116**, 1307 (2011).

[31] Y. Li, Z. Zhou, S. Zhang, and Z. Chen, J. Am. Chem. Soc. **130**, 16739 (2008).

[32] E. J. Santos, A. Ayuela, and D. Sánchez-Portal, J. Phys. Chem. C **116**, 1174 (2011).

[33] E. J. G. Santos, A. Ayuela, S. B. Fagan, J. Mendes Filho, D. L. Azevedo, A. G. Souza Filho, and D. Sánchez-Portal, Phys. Rev. B **78**, 195420 (2008).

[34] B. Huang, J. Yu, and S.-H. Wei, Phys. Rev. B **84**, 075415 (2011).

[35] Y. Li, Z. Zhou, P. Jin, Y. Chen, S. B. Zhang, and Z. Chen, J. Phys. Chem. C **114**, 12099 (2010).

[36] J. Zhou, L. Wang, R. Qin, J. Zheng, W. N. Mei, P. Dowben, S. Nagase, Z. Gao, and J. Lu, J. Phys. Chem. C **115**, 25273 (2011).

[37] E. Durgun, N. Akman, and S. Ciraci, Phys. Rev. B **78**, 195116 (2008).

[38] H. Sevinçli, M. Topsakal, E. Durgun, and S. Ciraci, Phys. Rev. B **77**, 195434 (2008).

[39] T. Yildirim, J. Íñiguez, and S. Ciraci, Phys. Rev. B **72**, 153403 (2005).

[40] S. Bertolazzi, J. Brivio, and A. Kis, ACS Nano **5**, 9703 (2011).

[41] H. Guo, N. Lu, L. Wang, X. Wu, and X. C. Zeng, J. Phys. Chem. C **118**, 7242 (2014).

[42] H. Zheng, B. Yang, D. Wang, R. Han, X. Du, and Y. Yan, Appl. Phys. Lett. **104**, 132403 (2014).

[43] L. Kou, C. Tang, Y. Zhang, T. Heine, C. Chen, and T. Frauenheim, J. Phys. Chem. Lett. **3**, 2934 (2012).

[44] Y. Ma, Y. Dai, M. Guo, C. Niu, Y. Zhu and B., and Huang, ACS Nano **6**, 1695 (2012).

[45] P. Manchanda, V. Sharma, H. Yu, D. J. Sellmyer, and R. Skomski, Appl. Phys. Lett. **107**, 032402 (2015).

[46] Y. Xu, X. Liu, and W. Guo, Nanoscale **6**, 12929 (2014).

[47] J. Lee, J. Huang, B. G. Sumpter, and M. Yoon, 2D Mater. **4**, 021016 (2017).

[48] J. Chen, Solid State Commun. **237**, 14 (2016).

[49] Y. Wang, C. Cong, C. Qiu, and T. Yu, Small **9**, 2857 (2013).

[50] See Supplemental Material at http://link.aps.org/supplemental/10.1103/PhysRevMaterials.3.084004 for the different spin configurations, lattice paratemeters, partial density of states, noncollinear phase, and phonon dispersion under strain and fitting parameters.

[51] Y. Ge and A. Y. Liu, Phys. Rev. B **86**, 104101 (2012).

[52] J.-A. Yan, M. A. Della. Cruz, B. Cook, and K. Varga, Sci. Rep. **5**, 16646 (2015).

[53] P. Johari and V. B. Shenoy, ACS Nano **6**, 5449 (2012).

[54] C.-Z. Chang, J. Zhang, X. Feng, J. Shen, Z. Zhang, M. Guo, K. Li, Y. Ou, P. Wei, and L.-L. Wang, Science **340**, 167 (2013).

[55] A. I. Liechtenstein, V. I. Anisimov, and J. Zaanen, Phys. Rev. B **52**, R5467(R) (1995).

[56] S. L. Dudarev, G. A. Botton, S. Y. Savrasov, C. J. Humphreys, and A. P. Sutton, Phys. Rev. B **57**, 1505 (1998).

[57] P. O. Löwdin, J. Chem. Phys. **18**, 365 (1950).

[58] J. Baker, Theor. Chim. Acta **68**, 221 (1985).

[59] R. F. W. Bader, *Atoms in Molecules a Quantum Theory* (Oxford University Press, Oxford, 1990).

[60] G. Henkelman, A. Arnaldsson, and H. Jónsson, Comput. Mater. Sci. **36**, 354 (2006).

[61] E. Sanville, S. D. Kenny, R. Smith, and G. Henkelman, J. Comput. Chem. **28**, 899 (2007).

[62] W. Tang, E. Sanville, and G. Henkelman, J. Phys. Condens. Matter **21**, 084204 (2009).

[63] M. F. Iozzi, T. Helgaker, and E. Uggerud, Mol. Phys. **107**, 2537 (2009).

[64] K. Binder and D. P. Landau, Phys. Rev. B **21**, 1941 (1980).

[65] L. Roelofs, in *Chemistry and Physics of Solid Surfaces IV* (Springer, Berlin, 1982), pp. 219.

[66] H. Jin, Y. Dai, B. Huang, and M.-H. Whangbo, Appl. Phys. Lett. **94**, 162505 (2009).

[67] P. Hajiyev, C. Cong, C. Qiu, and T. Yu, Sci. Rep. **3**, 2593 (2013).

[68] S. Sugai and K. Murase, Phys. Rev. B **25**, 2418 (1982).

[69] S. Gao, F. Flicker, R. Sankar, H. Zhao, Z. Ren, B. Rachmilowitz, S. Balachandar, F. Chou, K. S. Burch, Z. Wang, J. van Wezel, and I. Zeljkovic, Proc. Natl. Acad. Sci. **115**, 6986 (2018).

[70] D. Zhang, J. Ha, H. Baek, Y.-H. Chan, F. D. Natterer, A. F. Myers, J. D. Schumacher, W. G. Cullen, A. V. Davydov, and Y. Kuk, Phys. Rev. Mater. **1**, 024005 (2017).

[71] M. J. Wei, W. J. Lu, R. C. Xiao, H. Y. Lv, P. Tong, W. H. Song, and Y. P. Sun, Phys. Rev. B **96**, 165404 (2017).

[72] M. Bonilla, S. Kolekar, Y. Ma, H. C. Diaz, V. Kalappattil, R. Das, T. Eggers, H. R. Gutierrez, M.-H. Phan, and M. Batzill, Nat. Nanotechnol. **13**, 289 (2018).

[73] Y. Ge and A. Y. Liu, Phys. Rev. B **82**, 155133 (2010).

[74] H. Ryu, Y. Chen, H. Kim, H.-Z. Tsai, S. Tang, J. Jiang, F. Liou, S. Kahn, C. Jia, and A. A. Omrani, Nano Lett. **18**, 689 (2018).

[75] H. M. Hill, S. Chowdhury, J. R. Simpson, A. F. Rigosi, D. B. Newell, H. Berger, F. Tavazza, and A. R. Walker, Phys. Rev. B **99**, 174110 (2019).

[76] P. Hohenberg and W. Kohn, Phys. Rev. **136**, B864 (1964).

[77] W. Kohn and L. J. Sham, Phys. Rev. **140**, A1133 (1965).

[78] P. Giannozzi, S. Baroni, N. Bonini, M. Calandra, R. Car, C. Cavazzoni, D. Ceresoli, G. L. Chiarotti, M. Cococcioni, and I. Dabo, J. Phys. Condens. Matter **21**, 395502 (2009).

[79] G. Kresse and D. Joubert, Phys. Rev. B **59**, 1758 (1999).

[80] M. Methfessel and A. T. Paxton, Phys. Rev. B **40**, 3616 (1989).

[81] M. Yu and D. R. Trinkle, J. Chem. Phys. **134**, 064111 (2011).

[82] A. Dal Corso, Comput. Mater. Sci. **95**, 337 (2014).

[83] J. P. Perdew and A. Zunger, Phys. Rev. B **23**, 5048 (1981).

[84] J. P. Perdew, J. A. Chevary, S. H. Vosko, K. A. Jackson, M. R. Pederson, D. J. Singh, and C. Fiolhais, Phys. Rev. B **46**, 6671 (1992).

[85] N. D. Mermin, Phys. Rev. **137**, A1441 (1965).

[86] W. Kohn, Phys. Rev. Lett. **2**, 393 (1959).